ACS APPLIED MATERIALS & INTERFACES

Functional Inorganic Materials and Devices

Advent of Electrically Conducting Double-Helical Metal–Organic Frameworks Featuring Butterfly-Shaped Electron Rich #-Extended Tetrathiafulvalene Ligands

Monica A. Gordillo, Paola Andrea Benavides, Dillip K. Panda, and Sourav Saha

ACS Appl. Mater. Interfaces, **Just Accepted Manuscript** • DOI: 10.1021/acsami.9b20234 • Publication Date (Web): 07 Jan 2020

is published by the American Chemical Society. 1155 Sixteenth Street N.W., Washington, DC 20036

Advent of Electrically Conducting Double-Helical Metal–Organic Frameworks Featuring Butterfly-Shaped Electron Rich π-Extended Tetrathiafulvalene Ligands

Monica A. Gordillo, Paola A. Benavides, Dillip K. Panda, and Sourav Saha*

Department of Chemistry, Clemson University, Clemson, South Carolina 29634, United States

*Email: souravs@clemson.edu

ABSTRACT

In order to diversify metal–organic framework (MOF) structures beyond traditional Euclidean geometries and to create new charge delocalization pathways beneficial for electrical conductivity, we constructed a novel *double-helical* MOF (*dh*MOF) by introducing a new butterfly-shaped electron-rich π-extended tetrathiafulvalene ligand equipped with four benzoate groups (ExTTFTB). The face-to-face oriented convex ExTTFTB ligands connected by $Zn_2(COO)_4$ paddlewheel nodes formed ovoid cavities suitable for guest encapsulation, while π–π-interaction between the ExTTFTB ligands of neighboring strands helped create new charge delocalization pathways in iodine-mediated partially oxidized *dh*MOF. Iodine vapor diffusion led to oxidation of half of the ExTTFTB ligands in each double helical strand to $ExTTFTB^{\bullet+}$ radical cations, which putatively formed intermolecular ExTTFTB/$ExTTFTB^{\bullet+}$ π-donor/acceptor charge-transfer chains with the neutral ExTTFTB ligands of an adjacent strand, creating supramolecular wire-like charge delocalization pathways along the helix seams. In consequence, the electrical conductivity of *dh*MOF surged from 10^{-8} S/m up to 10^{-4} S/m range after iodine treatment. Thus, the introduction of electron rich ExTTFTB ligand with a distinctly convex π-surface not only afforded a novel double helical MOF architecture featuring ovoid cavities and unique charge delocalization pathways, but more importantly, delivered new tool and design strategy for future development of electrically conducting stimuli-responsive MOFs.

Keywords: double-helical MOFs • π-donor/acceptor interaction • electrical conductivity • π-extended tetrathiafulvalene • radical cation

INTRODUCTION

Owing to their diverse structures, compositions, and properties, metal–organic frameworks (MOFs)[1,2] have emerged as one of the most versatile functional materials with variety of applications ranging from size and shape selective separation,[3] storage,[4] and delivery[5] of guest entities to highly sophisticated electronic and ionic conduction,[6–10] energy storage,[11–14] light-harvesting,[15–19] catalysis,[20,21] and sensing[22–24]. Despite having tantalizing structural similarities with inorganic semiconductors, electrical conductivity (σ) remains one the most coveted but challenging features of porous MOFs.[8,9] The presence of high charge-carrier concentration and effective long-range charge-transport pathways are two essential prerequisites of this electronic property. Furnishing MOFs with redox-active building blocks[25] containing accessible electrons and holes is the vital first step toward engineering this desired property and may lead to remarkable conductivity when the resulting frameworks can support facile charge movement,[9,26–30] however, their presence alone does not necessarily guarantee electronic conductivity because insulating metal-cluster nodes and large inter-ligand distances often hinder long-range charge diffusion in porous MOFs. On the other hand, the porosity of MOFs could be exploited to manufacture this elusive property by introducing suitable guest molecules,[31] which could either oxidize or reduce the frameworks, producing mobile charge carriers,[32–38] or help create new charge delocalization pathways[39–43] that may not have been present in pristine materials.

Although tailoring MOF structures and properties for specific applications has always been a major focus of this burgeoning field, nearly all existing MOFs possessed classical Euclidean geometries defined by mostly linear and planar ligands.[1,2] Parallel studies elsewhere have demonstrated that large redox-active molecules with distinctly curved π-surfaces, such as fullerenes, carbon nanotubes, and corannulenes, enjoy relatively small electronic reorganization energy, i.e., they can accommodate additional charges acquired upon oxidation or reduction processes more easily than planar aromatics, a feature that is quite beneficial for various molecular electronics applications.[44] Yet, such ligands are extremely rare, and their potential benefits in MOFs remain practically unexplored. In an attempt to explore and exploit potential benefits of curved ligands in MOFs, Shustova and coworkers have recently introduced pyridyl-functionalized corannulene[45] and fullerene[46] ligands. However, only a shallow bowl-shaped tetrapyridyl-corannulene ligand yielded a clamshell Ag(I) coordination polymer,[45] while all other ligands essentially served as linear pillars in traditional MOF architectures. Therefore, there is a growing interest in easily accessible and scalable ligands with distinctive curved π-surfaces that could not only afford novel MOF architectures, but also help create novel charge delocalization pathways suitable for electrical conductivity and other fascinating properties.

Herein, we introduced for the first time a new butterfly-shaped electron rich π-extended tetrathiafulvalene ligand equipped with four benzoic acid units (ExTTFTB) to construct a novel *double-helical* MOF (*dh*MOF), which possessed large ovoid cavities capable of guest encapsulation and supramolecular wire-like charge delocalization pathways suitable for electrical conductivity (Figure 1a,b). Unlike planar TTF ligands containing four terminal benzoate or pyridyl groups that have been used in a number of different semiconducting MOFs,[27–29, 35–38] the ExTTF core[47–53] has a distinctly convex π-surface defined by a boat-shaped anthracene core bearing two 1,3-dithiolene rings at 9 and 10 positions located at a dihedral angle of ~81°.[48] Such a unique shape of ExTTFTB ligand not only led to the formation of a novel double-helical framework, but also helped create an unusual intermolecular π–π interaction between 1,3-dithiolene rings of neighboring double helical strands, which was distinct from those found in any other existing MOFs. In addition, unlike planar TTF compounds, which undergo stepwise one-electron oxidations to corresponding radical cations and dications, free and symmetrical ExTTF compounds undergo facile one-step two-electron oxidation to planar $ExTTF^{2+}$ dications.[49] However, in solid-state *dh*MOF, the convex shape of ExTTFTB ligands became highly constrained and its electron distribution become unsymmetrical due to non-symmetrical coordination environment of four carboxylate groups, which made the elusive $ExTTFTB^{\bullet+}$ radical cation state accessible. The EPR, XPS, electrochemical, and elemental analyses together demonstrated that iodine vapor diffusion oxidized half of the ExTTFTB ligands of each double helix to paramagnetic $ExTTFTB^{\bullet+}$ radical cations, which putatively formed intermolecular ExTTFTB/$ExTTFTB^{\bullet+}$ π-donor/acceptor chains (i.e., AEDAmers[54]) with the neutral ExTTFTB ligands of an adjacent strand (Figure 1c). Such π-donor/acceptor interactions not only mitigated the electrostatic repulsion between the partially oxidized *dh*MOF strands, but also facilitated through-space charge delocalization. As a result, the electrical conductivity of iodine-treated *dh*MOF surged to 2.6×10^{-4} S/m, a 10^4-fold improvement over that of pristine *dh*MOF (2×10^{-8} S/m).

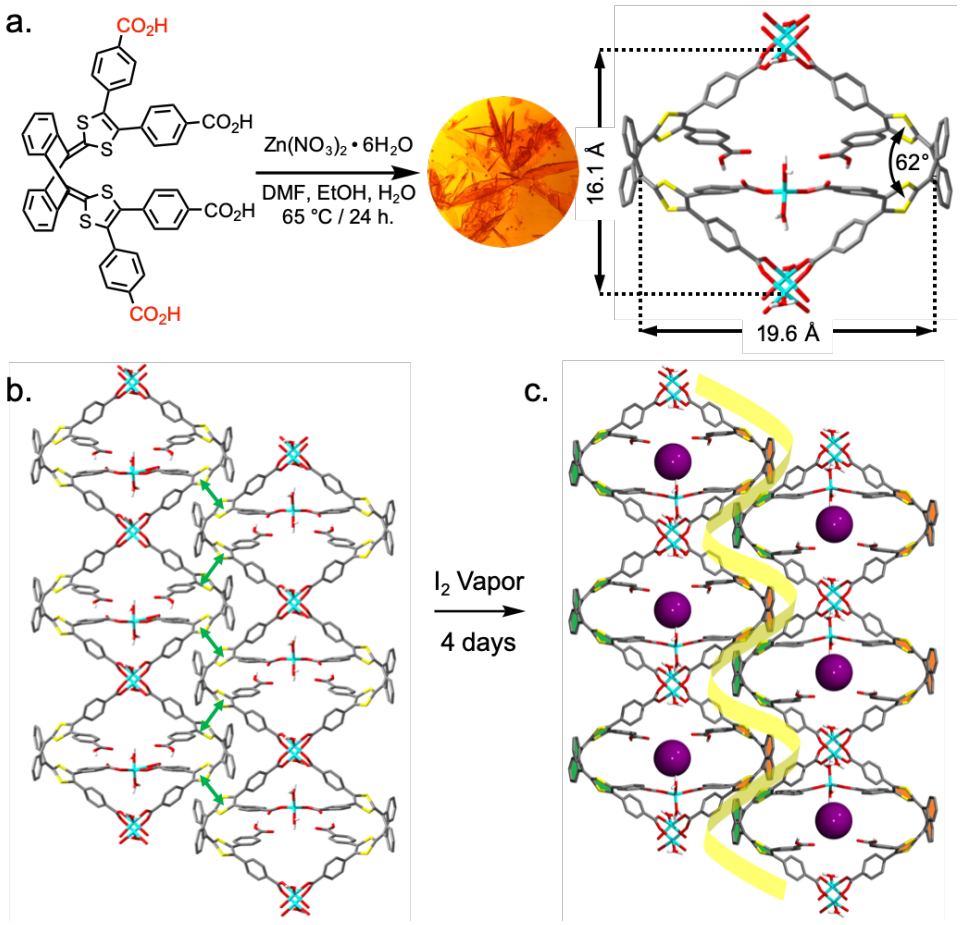

Figure 1. (a) Synthetic scheme and (b) SXRD structure of ExTTFTB-based *dh*MOF (C, grey; O, red; S, yellow; Zn, cyan; H-atoms and solvent molecules were omitted for clarity). The green arrows in (b) depict intermolecular distances between the ExTTFTB ligands of adjacent strands. (c) A proposed model of iodine-induced partially oxidized *dh*MOF depicting π-donor/acceptor chains made of neutral ExTTFTB ligands (orange space-filled) and ExTTFTB$^{\bullet+}$ radical cations (green space-filled) of neighboring strands that could facilitate charge delocalization and the possible location of I^- counterions (purple spheres, drawn to scale) inside the cavities.

RESULTS AND DISCUSSIONS

Synthesis and Structural Characterization of ExTTFTB-Based *dh*MOF. The orange colored ExTTFTB ligand was synthesized by a Pd-catalyzed cross-coupling reaction between ExTTF[47] core and ethyl-4-bromobenzoate,[51] followed by saponification of all four ester groups (Scheme S1). The ExTTF core was furnished with four benzoate groups because bidentate carboxylate groups usually form more stable and versatile multinuclear metal-cluster nodes than monodentate pyridyl groups, which should lead to chemically and structurally more robust MOF formation.

Solvothermal reaction between ExTTFTB ligand and $Zn_2(NO_3)_2 \cdot 6H_2O$ (~1:4 molar ratio) in a 3:3:2 DMF/EtOH/H_2O mixture (65 °C, 24 h) yielded orange plate-like *dh*MOF crystals (Figure 1). Single-crystal X-ray diffraction (XRD) analysis revealed a neutral double-helical MOF architecture $Zn_3(ExTTFTB)_2(H_2O)_4 \cdot 6EtOH$ (Figure 1) with $P\bar{1}$ space group. It contains large ovoid cavities (19.6 × 16.1 Å) surrounded by two face-to-face oriented ExTTFTB ligands linked by two $Zn_2(COO)_4$ paddlewheel nodes and a tetrahedral Zn(II) center in each loop. Only two opposite (C-*trans*) carboxylate groups of each ExTTFTB ligand are involved in the $Zn_2(COO)_4$ nodes formation, while the third one is singly coordinated to a tetrahedral Zn(II) and the fourth remains free and in the acid form. As a result of such coordination and rigidification of convex ExTTFTB ligand, its curvature became further accentuated in *dh*MOF, as the dihedral angle between the two 1,3-dithiolene rings shrunk to 62°. The parallel double-helical strands are aligned along the *a*-axis and packed in such a way that the convex ExTTF cores of a given strand bulge into the concave grooves of the two neighboring strands creating short intermolecular S···S distances (~3.8 Å) and π–π-interaction between the ExTTFTB ligands of adjacent strands. As demonstrated below, such supramolecular π–π-interactions between the ExTTFTB ligands in pristine *dh*MOF turned into intermolecular ExTTFTB/ExTTFTB$^{\bullet+}$ π-donor/acceptor chains upon iodine-mediated partial framework oxidation (Figure 1c), which further facilitated charge delocalization and improved its electrical conductivity.

The experimental powder X-ray diffraction (PXRD) pattern of activated pristine *dh*MOF (called **1** hereafter) was consistent with the simulated pattern (Figure 2a), confirming that the bulk material was phase-pure and retained its structural integrity upon activation thanks to the rigidity of convex ExTTFTB ligand. Like other iodine doped MOFs,[35,36,39] most of the PXRD peaks (Figure 2a) of iodine-treated and subsequently hexane-washed and evacuated material (called **1a** hereafter) appeared at the same positions as those displayed by pristine **1**, but became broader and weaker, suggesting that the framework remained mostly crystalline after iodine-mediated partial oxidation (*vide infra*).

Thermogravimetric analysis (TGA) coupled with differential scanning calorimetry (DSC) showed (Figure 2b) that **1** lost only 10% of initial weight before 200 °C due to the loss of residual solvent and then remained steady until 350 °C. Similarly, **1a** also lost only 10% of initial weight between 50–100 °C and then maintained a plateau until 350 °C, confirming that no excess iodine was present in this partially oxidized *dh*MOF beyond the requisite number of I^- anions to balance ExTTFTB$^{\bullet+}$ charges. In comparison, an iodine-treated and subsequently air-exposed but not washed material (called **1b** hereafter) suffered 17% weight loss between 50–150 °C indicating the loss of residual iodine, before holding steady until 350 °C. The DSC profiles showed no major phase transition in any of these materials before 350 °C. The Brunauer-Emmett-Teller (BET) surface area (66 m^2/g) and pore volume (5.1×10^{-2} cm^3/g) determined from CO_2-

sorption isotherms (Figure S1) indicated that *dh*MOF could host small guest molecules or ions. In contrast, the BET surface area and pore volume of iodine-treated partially oxidized **1a** diminished significantly (1.7 m^2/g and 2.4×10^{-2} cm^3/g, respectively) possibly because I^- counterions occupied the ovoid pores (*vide infra*). Nevertheless, based on PXRD data, the crystalline structure of iodine-treated *dh*MOF (**1a**) remained mostly intact.

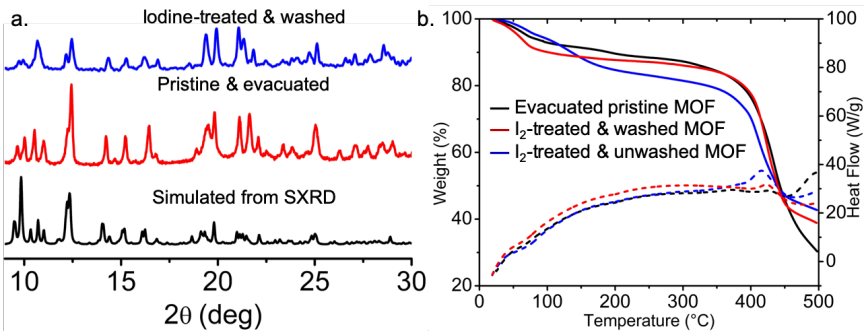

Figure 2. (a) PXRD patterns of pristine and iodine-treated *dh*MOFs. (b) TGA (solid) and DSC (dotted) profiles of pristine and iodine-treated *dh*MOF.

Electrochemical Behavior of Pristine and Iodine-Treated *dh*MOFs. Like other ExTTF compounds,[49] free ExTTFTB ligand also underwent (Figure 3a) a pseudoreversible one-step two-electron oxidation to $ExTTFTB^{2+}$ dication displaying an anodic peak at 0.66 and a cathodic peak at 0.34 V (E_{Ox} = 0.50 V vs. Ag/AgCl in 0.1 M Bu_4NPF_6 / DMF). In contrast, the cyclic voltammogram (CV) of pristine *dh*MOF (**1**) thin-film drop-cast on a glassy carbon electrode displayed (Figures 3b and c) two distinct anodic peaks at 0.50 and 0.66 V (*vs.* Ag/AgCl, 0.1 M Bu_4NPF_6 in MeCN), indicating stepwise one-electron oxidation of the MOF-bound ExTTFTB ligand to $ExTTFTB^{\bullet+}$ radical cation and $ExTTFTB^{2+}$ dication. These results demonstrate that although free $ExTTFTB^{\bullet+}$ radical cation was not accessible in solution, the nonsymmetrical coordination environment of four carboxylate groups of ExTTFTB ligands in *dh*MOF (two *trans* carboxylate groups formed Zn_2 paddlewheel nodes, the third one coordinated with a tetrahedral Zn(II) site, and the fourth remained free and protonated) desymmetrized its electron distribution, which led to separation of the two oxidation steps and rendered the $ExTTFTB^{\bullet+}$ radical cation state accessible. Furthermore, in *dh*MOF, the convex ExTTFTB ligands were rigidified and their curvature became more pronounced, which likely impacted their redox behavior. Although free ExTTF compounds turn into planar $ExTTFTB^{2+}$ dication upon two-electron oxidation,[49,50] previous studies[51,52] showed that symmetrical metallocages consisting of two convex tetrapyridyl-ExTTF (TPExTTF) ligands connected by four bis(diphenylphosphino)ferrocene-capped Pt(II) or Pd(II) centers remained intact even after two-electron oxidation of both TPExTTF ligands to corresponding dications, suggesting that it is also possible for

*dh*MOF to retain its structure after oxidation of ExTTFTB ligands. The anodic peaks of iodine-treated **1a** (Figures 3b and d) appeared at more positive potentials (0.53 and 0.74 V *vs.* Ag/AgCl, 0.1 M Bu_4NPF_6 in MeCN) than pristine **1**, suggesting that iodine-mediated oxidation of some ExTTFTB ligands to $ExTTFTB^{\bullet+}$ radical cations and ensuing intermolecular ExTTFTB/$ExTTFTB^{\bullet+}$ charge-transfer interaction (Figure 1c) made electrochemical oxidation of this partially oxidized material more difficult than the free ligand and pristine *dh*MOF. To probe framework stability during electrochemical oxidation, multiple CV cycles of **1** and **1a** were recorded, which displayed good agreement among the repetitive cycles (Figures S2), suggesting that both materials were stable under these conditions.

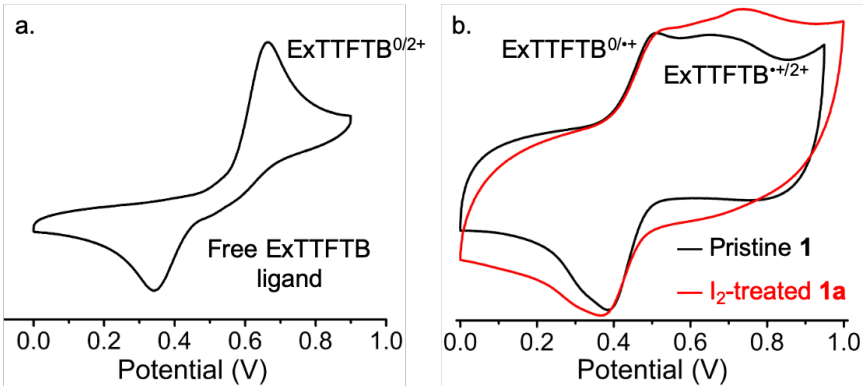

Figure 3. The cyclic voltammograms of (a) free ExTTFTB ligand (*vs.* Ag/AgCl, 0.1 M Bu_4NPF_6 in DMF) and (b–d) pristine **1** (black traces) and iodine-treated **1a** (red traces) (*vs.* Ag/AgCl, 0.1 M Bu_4NPF_6 in MeCN). The repetitive cycles in (c) and (d) indicate framework stability during electrochemical oxidation.

EPR and XPS Analyses of Pristine and Iodine-Treated Partially Oxidized *dh*MOFs. The presence of paramagnetic $ExTTFTB^{\bullet+}$ radical cations and I^- counterions in iodine-mediated partially oxidized **1a** was revealed by EPR and X-ray photoemission spectroscopies, respectively. The solid-state EPR spectrum of **1** showed a negligible signal (Figure 4a), indicating that the majority of ExTTFTB ligands remained in the neutral state, although few may have been partially oxidized by air, as found in other tetrathiafulvalene-based MOFs.[26–28, 35–38] In contrast, **1a** displayed (Figure 3b) a strong EPR signal ($g \approx 2.005$), demonstrating that a large number of ExTTFTB ligands were indeed oxidized to paramagnetic $ExTTFTB^{\bullet+}$ radical cations. The EPR data further confirmed that iodine oxidized some ExTTFTB ligands only to $ExTTFTB^{\bullet+}$ radical cations, not to diamagnetic $ExTTFTB^{2+}$ dications. The iodine-mediated oxidation of ExTTFTB ligands to $ExTTFTB^{\bullet+}$ radical cations should also generate I^- counterions to complete the redox reaction and to maintain charge balance in partially oxidized *dh*MOF (**1a**). The XPS analysis of **1a** displayed (Figure 4b) characteristic I^- peaks at 617.6 (I $3d_{5/2}$) and 628.9 (I $3d_{3/2}$) eV,[55,56] but no such peak was displayed by **1**.

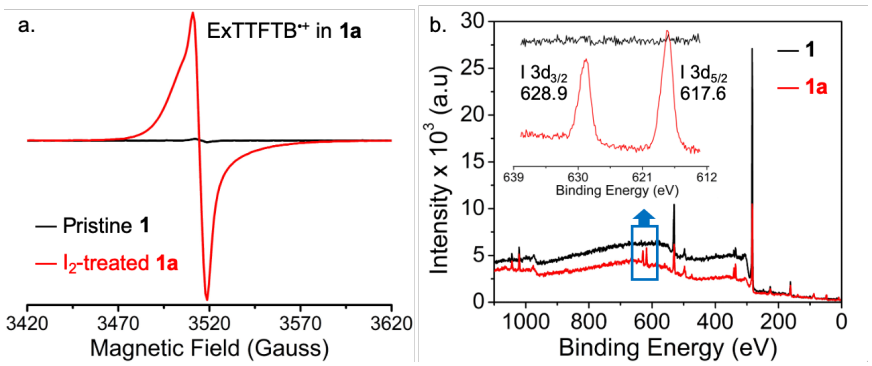

Figure 4. (a) Solid-state EPR spectra of pristine **1** (black) and iodine-treated **1a** (red). (b) The survey XPS and high resolution I 3d XPS (inset) show characteristic I^- peaks in **1a** (red) but not in **1** (black).

Elemental Analysis of Pristine and Iodine-Treated *dh*MOFs. The amount of ExTTFTB$^{\bullet+}$ radical cations in **1a**, which must be accompanied by an equal number of charge-balancing I^- counterions, was estimated from elemental analysis. This insight, together with the crystal structure of *dh*MOF, allowed us to depict the most plausible arrangement of these species and a potential charge delocalization pathway in **1a** (Figure 1c). The elemental analysis data of **1a** (C 52.78%, H 3.59%, S 10.84%, and I 5.91%) corresponds to an empirical formula of $Zn_3C_{100}H_{78}O_{26}S_8I$. Based on the S:I ratio, **1a** contains one I^- anion for each pair of ExTTTB ligands, i.e., the ExTTFTB to I^- ratio is 2:1. That means only half of the ExTTFTB ligands, possibly one in each loop is oxidized to an ExTTFTB$^{\bullet+}$ radical cation, which is accompanied by an I^- counterion. The crystal structure of *dh*MOF (Figure 1) shows that the ovoid cavities are large enough to accommodate one I^- anion (diameter 3.96 Å) inside each cavity, whereas the gaps between double helical strands (~3.8 Å) are too narrow for them, suggesting that the ovoid cavities are the most likely location of I^- counterions in **1a** (Figure 1c). Attempt to determine the single crystal structure of iodine-treated *dh*MOF (**1a**) was not successful as the crystals diffracted poorly, however, the PXRD pattern and physical appearance suggested that it remained crystalline.

Taken together, these experimental results suggested that about half of the ExTTFTB ligands in **1a** were oxidized to ExTTFTB$^{\bullet+}$ radical cations, which were accompanied by an equal number of I^- anion. Based on this information and the crystal structure of *dh*MOF, we postulated that the iodine-generated ExTTFTB$^{\bullet+}$ radical cations of a given strand and the neutral ExTTFTB ligands of an adjacent strand, which are technically located only ~3.8 Å apart, would form extended π-donor/acceptor chains along the seams of the neighboring strands (Figure 1c). Such intermolecular ExTTFTB/ExTTFTB$^{\bullet+}$ π-donor/acceptor CT interactions would not only stabilize the partially oxidized *dh*MOF and hinder the oxidation of all ExTTFTB ligands, but also create unique charge delocalization pathways along the seams of adjacent stands that could be beneficial for long-range charge delocalization and electrical conductivity of iodine-treated *dh*MOF.

While we considered other possible arrangements of ExTTFTB$^{\bullet+}$ in **1a**, the proposed model (Figure 1c) depicting the formation of supramolecular ExTTFTB/ExTTFTB$^{\bullet+}$ chains along the seams of *dh*MOF strands is the most plausible one since it provides the greatest stabilization to partially oxidized *dh*MOF by minimizing the electrostatic repulsion between ExTTFTB$^{\bullet+}$ radical cations more effectively than any other arrangements. For instance, the convex ExTTFTB ligands in a given double helical strand are located too far apart to allow any meaningful stabilizing interaction between the neutral and oxidized ligands. Similarly, an alternating arrangement of neutral and singly oxidized ExTTFTB ligands between the left and right sides of a given double helical strand of **1a** (as opposed to all neutral ligands being one side and all ExTTFTB$^{\bullet+}$ on the other) would create electrostatic repulsion between the adjacent ExTTFTB$^{\bullet+}$ radical cations of neighboring strands, leaving the proposed model depicted in Figure 1c the most reasonable one.

Optical Spectra and Band Gaps of Pristine and Iodine-Treated *dh*MOFs. The UV-Vis absorption spectrum of free ExTTFTB ligand (Figure 5a) displayed the longest wavelength absorption peak at 445 nm. From the onset of this peak, its optical band gap was estimated to be 2.6 eV. The diffuse reflectance spectra (DRS) of **1** and **1a** (Figure 5b) featured the longest wavelength absorption peaks at 480 and 630 nm, respectively, from which their respective optical band gaps of 2.2 and 1.7 eV were estimated. Thus, the optical band gaps of both **1** and **1a** were much narrower than that of free ExTTFTB ligand, which can be attributed to intermolecular π–π and π-donor/acceptor interactions in pristine and iodine-mediated partially oxidized *dh*MOFs, respectively. The corresponding Tauc plots provided further insights into their respective direct and indirect band gaps (Figures 5c and d),[57] which were in good agreement with those determined from DRS and confirmed that partially oxidized **1a** indeed enjoyed ~0.5 eV narrower band gap than neutral **1** possibly due to intermolecular ExTTFTB/ExTTFTB$^{\bullet+}$ π-donor/acceptor interaction in the former.

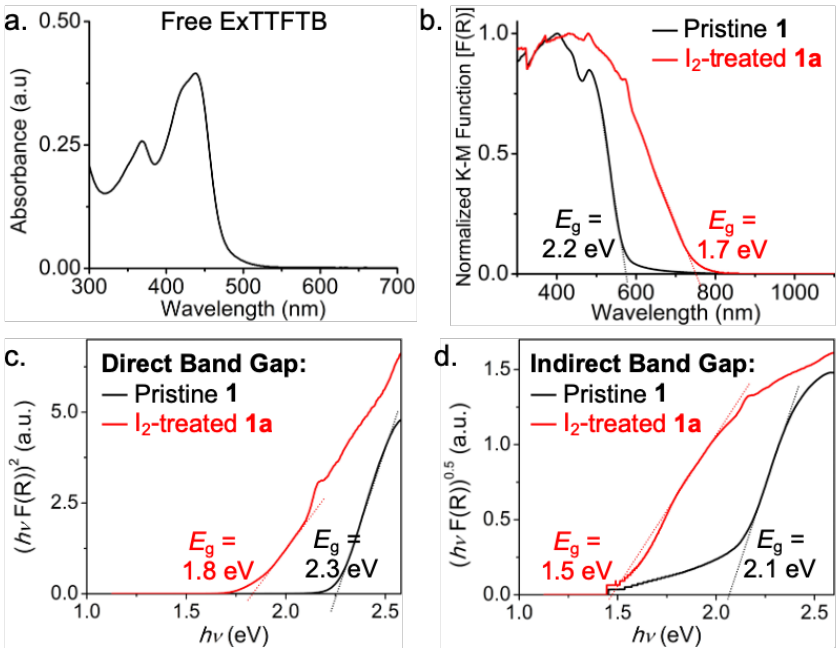

Figure 5. (a) UV-Vis absorption spectrum of free ExTTFTB ligand in DMF. (b) Diffusion reflectance spectra of **1** (black) **1a** (red). (c, d) The Tauc plots of **1** (black) **1a** (red) revealed their respective direct (c) and indirect (d) band gaps.

Electrical Conductivity of Pristine and Iodine-Treated *dh*MOFs. Finally, the electrical conductivities of pristine and iodine-treated *dh*MOFs were determined from *dc*-sweep and EIS measurements performed on *in-situ* pressed MOF pellets sandwiched between two conductive-C or Ag-coated stainless-steel electrodes (Table 1).[14,58,59] Irrespective of the electrodes, all three materials (i.e., **1**, **1a**, and **1b**) displayed linear current-voltage (*I-V*) profiles between –1 to +1 V (Figure 6), confirming electrical current and ohmic contact between the pellets and electrodes. Based on the slopes of respective *I-V* plots, the electrical conductivity of **1b** (~10^{-4} S/m) was found to be 10^4 times greater than that of **1** (~10^{-8} S/m), while that of **1a** (~10^{-6} S/m) lied between the two materials. Fully consistent with these results, the Nyquist plots (Figure S3) obtained from EIS measurements also revealed the same trend and similar σ-values of the respective materials (Table 1). The electrical conductivities of **1a** and **1b** were 10–1000 times greater than that of iodine (10^{-7} S/m), confirming that the iodine-treated *dh*MOFs were indeed responsible for electrical conduction. The iodine-induced ~100-fold conductivity enhancement in **1a** (devoid of excess iodine except I^- counterions needed to balance the ExTTFTB$^{\bullet+}$ charge) could be attributed to partial framework oxidation, which not only increased the charge-carrier concentration, but also facilitated charge delocalization through the proposed ExTTFTB/ExTTFTB$^{\bullet+}$ chains formed along the seams of neighboring strands (Figure 1c). In contrast, **1b** contained additional iodine molecules (based on the TGA data), which likely contributed to its

even higher conductivity by facilitating electron movement across the grain boundaries. Thus, the unique structural features of *dh*MOF enabled us to engineer a desired feature through guest infiltration, which was not fully expressed in the pristine material. It is worth noting that the bulk electrical conductivity value measured with pelletized sample is usually underestimated from the intrinsic conductivity of the material due to undeterminable contributions of grain-boundary and contact resistance. The PXRD patterns of pelletized **1** and **1a** recorded before and after electrical measurements were in good agreement (Figure S4), indicating that these materials remained stable under these conditions.

Table 1. Electrical conductivity (S/m) of 1, 1a, and 1b measured by direct-current (*dc*) sweep and electrochemical impedance spectroscopy (EIS) using MOF pellets sandwiched between two stainless-steel electrodes coated with conductive-C[a] and Ag[b] paints.

	1	1a	1b
dc-sweep[a]	3.0×10^{-8}	1.3×10^{-6}	3.2×10^{-4}
dc-sweep[b]	1.9×10^{-8}	2.4×10^{-7}	2.6×10^{-4}
EIS[b]	2.5×10^{-8}	1.8×10^{-6}	2.7×10^{-4}

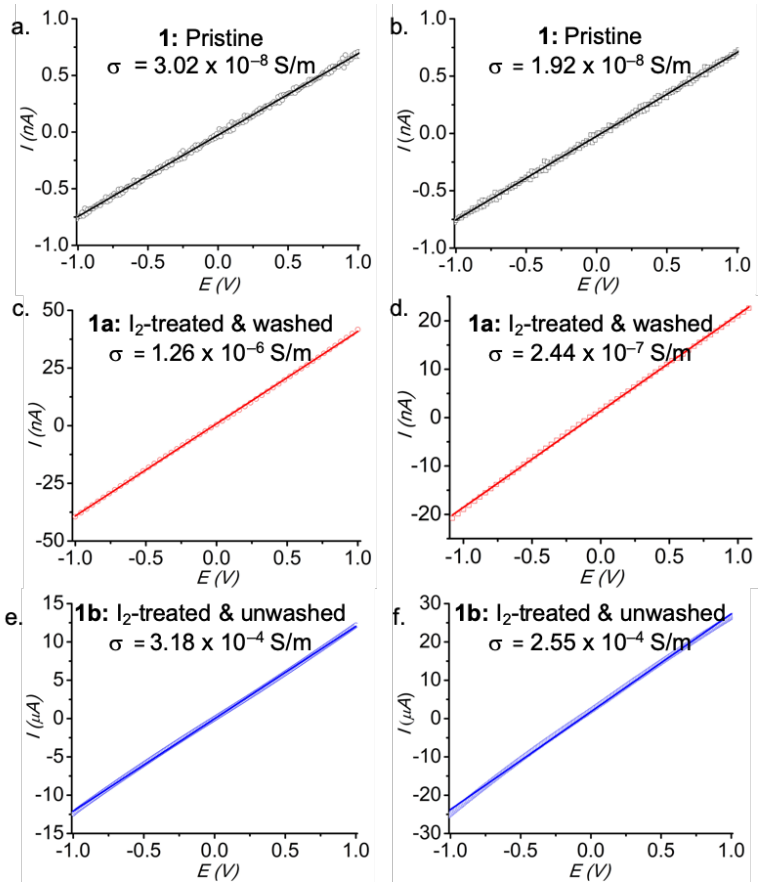

Figure 6. The linear *I-V* relationships of **1** (black), **1a** (red), and **1b** (blue) measured using conductive-C (left panel) and Ag-coated (right panel) stainless-steel electrodes.

CONCLUSIONS

In summary, we have developed a novel double-helical MOF architecture by introducing a new electron rich convex ExTTFTB ligand, which helped create a unique through-space charge-delocalization pathway suitable for electrical conductivity. The iodine-mediated partial framework oxidation boosted its electrical conductivity up to 10^{-4} S/m range, over 10^4 times above the pristine *dh*MOF's, which could be attributed to facile charge delocalization through ExTTFTB/ExTTFTB$^{\bullet+}$ π-donor/acceptor chains formed along the seams of *dh*MOF strands. Most importantly, by introducing ExTTF ligand, this work presents new tools and design strategies for the development of other double-helical MOFs with unique through-space charge movement pathways, which could be useful for myriad molecular electronics applications.

ASSOCIATED CONTENT

Supporting Information

The Supporting Information is available free of charge on the ACS Publications website at DOI: XXXXX. Experimental details including materials and methods, synthetic protocols, characterization, device construction and electrical measurement techniques, additional data (PDF), and CIF files.

AUTHOR INFORMATION

*Corresponding Author

Email: souravs@clemson.edu

ORCID

Sourav Saha: 0000-0001-6610-4820

Note

The authors declare no competing financial interest.

ACKNOWLEDGEMENTS

This work was supported by the National Science Foundation (award no. DMR-1809092 and CHE-1660329) and Clemson University. We thank Dr. Collin McMillen for assistance with single crystal x-ray analysis.

REFERENCES

1. Furukawa, H.; Cordova, K. E.; O'Keeffe, M.; Yaghi, O. M. The Chemistry and Applications of Metal-Organic Frameworks. *Science* **2013**, *341*, 974–986.
2. Yuan, S.; Feng, L.; Wang, K.; Pang, J.; Bosch, M.; Lollar, C.; Sun, Y.; Qin, J.; Yang, X.; Zhang, P.; Wang, Q.; Zou, L.; Zhang, Y.; Zhang, L.; Fang, Y.; Li, J.; Zhou, H.-C. Stable Metal–Organic Frameworks: Design, Synthesis, and Applications. *Adv. Mater.* **2018**, *30*, 1704303 (1–35).
3. Li, J.-R.; Sculley, J.; Zhou, H.-C. Metal–Organic Frameworks for Separations. *Chem. Rev.* **2012**, *112*, 869–932.
4. Sumida, K.; Rogow, D. L.; Mason, J. A.; McDonald, T. M.; Bloch, E. D.; Herm, Z. R.; Bae, T.-H.; Long, J. R., Carbon Dioxide Capture in Metal–Organic Frameworks. *Chem. Rev.* **2012**, *112*, 724–781.
5. Horcajada, P.; Gref, R.; Baati, T.; Allan, P. K.; Maurin, G.; Couvreur, P.; Férey, G.; Morris, R. E.; Serre, C. Metal–Organic Frameworks in Biomedicine. *Chem. Rev.* **2012**, *112*, 1232–1268.
6. Horike, S.; Umeyama, D.; Kitagawa, S., Ion Conductivity and Transport by Porous Coordination Polymers and Metal-Organic Frameworks. *Acc. Chem. Res.* **2013,** *46*, 2376–2384.
7. Ramaswamy, P.; Wong, N. E.; Shimizu, G. K. H., MOFs as Proton Conductors — Challenges and Opportunities. *Chem. Soc. Rev.* **2014**, *43*, 5913–5932.
8. Stavila, V.; Talin, A. A.; Allendorf, M. D. MOF-Based Electronic and Optoelectronic Devices. *Chem. Soc. Rev.* **2014**, *43*, 5994-6010.
9. Sun, L.; Campbell, M. G.; Dincă, M. Electrically Conductive Porous Metal–Organic Frameworks. *Angew. Chem. Int. Ed.* **2016**, *55*, 3566–3579.
10. Stassen, I.; Burtch, N.; Talin, A.; Falcaro, P.; Allendorf, M.; Ameloot, R. An Updated Roadmap for the Integration of Metal–Organic Frameworks with Electronic Devices and Chemical Sensors. *Chem. Soc. Rev.* **2017**, *46*, 3185–3241.
11. Wang, L.; Han, Y. Z.; Feng, X.; Zhou, J. W.; Qi, P. F.; Wang, B., Metal-organic frameworks for energy storage: Batteries and supercapacitors. *Coord. Chem. Rev.* **2016,** *307*, 361–381.
12. Wang, H.; Zhu, Q.-L.; Zou, R.; Xu, Q. Metal–Organic Frameworks for Energy Applications. *Chem* **2017**, *2*, 52–80.
13. Park, S. S.; Tulchinsky, Y.; Dincă, M. Single-Ion Li^+, Na^+, and Mg^{2+} Solid Electrolytes Supported by a Mesoporous Anionic Cu−Azolate Metal−Organic Framework. *J. Am. Chem. Soc.* **2017***, 139,* 13260−13263.

14. Panda, D. K.; Maity, K.; Palukoshka, A.; Ibrahim, F.; Saha, S. Li^{+} Ion-Conducting Sulfonate-Based Neutral Metal–Organic Framework. *ACS Sus. Chem. Eng*. **2019**, *7*, 4619–4624.

15. So, M. C.; Weiderrecht, G. P.; Mondloch, J. E.; Hupp, J. T.; Farha, O. K. Metal–Organic Framework Materials for Light-Harvesting and Energy Transfer. *Chem. Commun.* **2015**, *51*, 3501–3510.

16. Liu, J.; Zhou, W.; Liu, J.; Howard, I.; Kilibarda, G.; Schlabach, S.; Coupry, D.; Addicoat, M.; Yoneda, S.; Tsutsui, Y.; Sakurai, T.; Seki, S.; Wang, Z.; Lindemann, P.; Redel, E.; Heine, T.; Wöll, C. Photoinduced Charge-Carrier Generation in Epitaxial MOF Thin Films: High Efficiency as a Result of an Indirect Electronic Band Gap? *Angew. Chem. Int. Ed.* **2015**, *54*, 7441–7445.

17. Maza, W.A.; Haring, A. J.; Ahrenholtz, S. R.; Epley, C. C.; Lin, S. Y.; Morris, A. J. Ruthenium(II)-Polypyridyl Zirconium(IV) Metal–Organic Frameworks As a New Class of Sensitized Solar Cells. *Chem. Sci.* **2016**, *7*, 719–727.

18. Gordillo, M. A.; Panda, D. K.; Saha, S. Efficient MOF-Sensitized Solar Cells Featuring Solvothermally Grown [100]-Oriented Pillared Porphyrin Framework-11 Films on ZnO/FTO Surfaces. *ACS Appl. Mater. Interfaces* **2019**, *11*, 3196–3206.

19. Zhang, T.; Lin, W. Metal–Organic Frameworks for Artificial Photosynthesis and Photocatalysis. *Chem. Soc. Rev.* **2014**, *43*, 5982–5993.

20. Liu, J.; Chen, L.; Cui, H.; Zhang, J.; Zhang, L.; Su, C.-Y. Application of Metal–Organic Frameworks in Heterogeneous Supramolecular Catalysis. *Chem. Soc. Rev.* **2014**, *43*, 6011–6061.

21. Dolgopolova, E. A.; Shustova, N. B. Metal-Organic Framework Photophysics: Optoelectronic Devices, Photoswitches, Sensors, and Photocatalysts. *MRS Bulletin* **2016**, *41*, 890–896.

22. Lustig, W. P.; Mukherjee, S.; Rudd, N, D.; Desai, A. V.; Li, J.; Ghosh, S. K., Metal–Organic Frameworks: Functional Luminescent and Photonic Materials for Sensing Applications. *Chem. Soc. Rev.* **2017**, *46*, 3241–3235.

23. Khatun, A.; Panda, D. K.; Sayresmith, N.; Walter, M. G.; Saha, S. Thiazolothiazole-Based Luminescent Metal–Organic Frameworks with Ligand-to-Ligand Energy Transfer and Hg^{2+}-Sensing Capabilities. *Inorg. Chem.* **2019**, *58*, 12707–12715.

24. D'Alessandro, D. M. Exploiting Redox Activity in Metal–Organic Frameworks: Concepts, Trends and Perspectives. *Chem. Commun.* **2016**, *52*, 8957–8971.

25. Leong, C. F.; Usov, P. M.; D'Alessandro, D. M. Intrinsically Conducting Metal-Organic Frameworks. *MRS Bulletin* **2016**, *41*, 858–864.

26. Narayan, T. C.; Miyakai, T.; Seki, S.; Dincă, M.; High Charge Mobility in a Tetrathiafulvalene-Based Microporous Metal−Organic Framework. *J. Am. Chem. Soc*. **2012***, 134,* 12932–12935.

27. Park, S. S.; Hontz, E. R.; Sun, L.; Hendon, C. H.; Walsh, A.; Van Voorhis, T.; Dincă, M. Cation-Dependent Intrinsic Electrical Conductivity in Isostructural Tetrathiafulvalene-Based Microporous Metal–Organic Frameworks. *J. Am. Chem. Soc.* **2015**, *137*, 1774–1777.

28. Xie, L. S.; Alexandrov, E. V.; Skorupskii, G.; Proserpio, D. M.; Dincă, M. Diverse π–π stacking motifs modulate electrical conductivity in tetrathiafulvalene-based metal–organic frameworks. *Chem. Sci.* **2019**, *10*, 8558–8565.

29. Sheberla, D.; Sun, L.; Blood-Forsythe, M. A.; Er, S.; Wade, C. R.; Brozek, C. K. Aspuru-Guzik, A.; Dincă, M.; High Electrical Conductivity in Ni_3(2,3,6,7,10,11-hexaiminotriphenylene)$_2$, a Semiconducting Metal−Organic Graphene Analogue. *J. Am. Chem. Soc*. **2014**, *136*, 8859–8862.

30. Dou, J.; Sun, L.; Ge, Y.; Li, W.; Hendon, C. H.; Li, J.; Gul, S.; Yano, J.; Stach, E. A.; Dincă, M., Signature of Metallic Behavior in the Metal–Organic Frameworks M_3(hexaiminobenzene)$_2$ (M = Ni, Cu). *J. Am. Chem. Soc.* **2017**, *139*, 13608–13611.

31. Ullman, A. M.; Brown, J. W.; Foster, M. E.; Léonard, F.; Leong, K.; Stavila, V.; Allendorf, M. D. Transforming MOFs for Energy Applications Using Guest@MOF Concept. *Inorg. Chem.* **2016**, *55*, 7233–7249.

32. Kobayashi, Y.; Jacobs, B.; Allendorf, M. D.; Long, J. R., Conductivity, Doping, and Redox Chemistry of a Microporous Dithiolene-Based Metal–Organic Framework. *Chem. Mater.* **2010**, *22*, 4120–4122.

33. Gandara, F.; Uribe-Romo, F. J.; Britt, D. K.; Furukawa, H.; Lei, L.; Cheng, R.; Duan, X.; O'Keeffe, M.; Yaghi, O. M. Porous, Conductive Metal-Triazolates and Their Structural Elucidation by the Charge-Flipping Method. *Chem. Eur. J.* **2012**, *18*, 10595–10601.

34. Cai, S.-L.; Zhang, Y.-B.; Pun, A. B.; He, B.; Yang, J.; Toma, F. M.; Sharp, I. D.; Yaghi, O. M.; Fan, J.; Zheng, S.-R.; Zhang, W.-G.; Liu, Y. Tunable Electrical Conductivity in Oriented Thin Films of Tetrathiafulvalene-Based Covalent Organic Framework. *Chem. Sci.* **2014**, *5*, 4693–4700.

35. Wang, H.-Y.; Ge, J.-Y.; Hua, C.; Jiao, C.-Q.; Wu, Y.; Leong, C. F.; D'Alessandro, D. M.; Liu, T.; Zuo, J.-L. Photo- and Electronically Switchable Spin-Crossover Iron(II) Metal-Organic Frameworks Based on a Tetrathiafulvalene Ligand. *Angew. Chem. Int. Ed.* **2017**, *56*, 5465–5470.

36. Leong, C. F.; Wang, C.-H.; Ling, C. D.; D'Alessandro, D. M. A Spectroscopic and Electrochemical Investigation of a Tetrathiafulvalene Series of Metal–Organic Frameworks. *Polyhedron* **2018**, *154*, 334–342.

37. Su, J.; Hu, T.-H.; Murase, R.; Wang, H.-Y.; D'Alessandro, D. M.; Kurmoo, M.; Zuo, J.-L. Redox Activities of Metal–Organic Frameworks Incorporating Rare-Earth Metal Chains and Tetrathiafulvalene Linkers. *Inorg. Chem.* **2019**, *58*, 3698–3706.

38. Su, J.; Yuan, S.; Wang, H.-Y.; Huang, L.; Ge, J.-Y.; Joseph, E.; Qin, J.; Cagin, T.; Zuo, J.-L.; Zhou, H.-C. Redox-Switchable Breathing Behavior in Tetrathiafulvalene-Based Metal–Organic Frameworks. *Nat. Commun.* **2017**, *8*, 2008–2016.

39. Zeng, M.-H.; Wang, Q.-X.; Tan, Y.-X.; Hu, S.; Zhao, H.-X.; Long, L.-S.; Kurmoo, M. Rigid Pillars and Double Walls in a Porous Metal-Organic Framework: Single-Crystal to Single-Crystal, Controlled Uptake and Release of Iodine and Electrical Conductivity. *J. Am. Chem. Soc.* **2010**, *132*, 2561–2563.

40. Talin, A. A.; Centrone, A.; Ford, A. C.; Foster, M. E.; Stavila, V.; Haney, P.; Kinney, R. A.; Szalai, V.; Gabaly, F. E.; Yoon, H. P.; Léonard, F.; Allendorf, M. D. Tunable Electrical Conductivity in Metal-Organic Framework Thin-Film Devices. *Science* **2014**, *343*, 66–69.

41. Guo, Z.; Panda, D. K.; Maity, K.; Lindsey, D.; Parker, T. G.; Albrecht-Schmitt, T. E.; Barreda-Esparza, J. L.; Xiong, P.; Zhou, W.; Saha, S. Modulating Electrical Conductivity of Metal–Organic Framework Films with Intercalated Guest π-Systems. *J. Mater. Chem. C* **2016**, *4*, 894–899.

42. Guo, Z.; Panda, D. K.; Gordillo, M. A; Khatun, A.; Wu, H.; Zhou, W.; Saha, S. Lowering Band Gap of an Electroactive Metal–Organic Framework via Complementary Guest Intercalation. *ACS Appl. Mater. Interfaces* **2017**, *9*, 32413–32417.

43. Goswami, S.; Ray, D.; Otake, K.-I.; Kung, C.-W.; Garibay, S. J.; Islamoglu, T.; Atilgan, A.; Cui, Y.; Cramer, C. J.; Farha, O. K.; Hupp, J. T. A Porous, Electrically Conductive Hexa-Zirconium(IV) Metal–Organic Framework. *Chem. Sci*. **2018**, *9*, 4477–4482.

44. Pinzón, J. R.; Villalta-Cedres, A.; Echegoyen, L. Fullerenes, carbon nanotubes, and graphene for molecular electronics. *Top. Curr. Chem*. **2012**, *312*, 127–174.

45. Rice, A. M.; Fellows, W. B.; Dolgopolova, E. A.; Greytak, A. B.; Vannucci, A. K.; Smith, M. D.; Karakalos, S. G.; Krause, J. A.; Avdoshenko, S. M.; Popov, A. A.; Shustova, N. B. Hierarchical Corannulene-Based Materials: Energy Transfer and Solid-State Photophysics. *Angew. Chem. Int. Ed.* **2017**, *56*, 4525–4529.

46. Williams, D. E.; Dolgopolova, E. A.; Godfrey, D. C.; Ermolaeva, E. D.; Pellechia, P. J.; Greytak, A. B.; Smith, M. D.; Avdoshenko, S. M.; Popov, A. A.; Shustova, N. B. Fulleretic Well-Defined Scaffolds: Donor-Fullerene Alignment Through Metal Coordination and Its Effect on Photophysics. *Angew. Chem. Int. Ed.* **2016**, *55*, 9070–9074.

47. Yamashita, Y.; Kobayashi, Y.; Miyashi, T. *p*-Quinodimethane Analogues of Tetrathiafulvalene. *Angew. Chem. Int. Ed.* **1989**, *28*, 1052–1053.

48. Ren, Y.; Lee, S.; Bertke, J. A.; Moore, J. S. Crystal Structure of 9,10-Bis(1,3-Dithiol-2-Ylidene)-9,10-Dihydroanthracene. *Acta Crystallogr. Sect. E Crystallogr. Commun.* **2015**, *71*, 1475–1479.

49. Brunetti, F. G.; López, J. L.; Atienza, C.; Martín, N. π-Extended TTF: A Versatile Molecule for Organic Electronics. *J. Mater. Chem.* **2012**, *22*, 4188-4205.

50. Jana, A.; Bähring, S.; Ishida, M.; Goeb, S.; Canevet, D.; Sallé, M.; Jeppesen, J. O.; Sessler, J. L. Functionalized Tetrathiafulvalene- (TTF-) Macrocycles: Recent Trends in Applied Supramolecular Chemistry. *Chem. Soc. Rev.* **2018**, *47*, 5614–5645.

51. Bivaud, S.; Goeb, S.; Croué, V.; Dron, P. I.; Allain, M.; Sallé, M. Self-Assembled Containers Based on Extended Tetrathiafulvalene. *J. Am. Chem. Soc.* **2013**, *135*, 10018–10021.

52. Croué, V.; Goeb, S.; Szalóki, G.; Allain, M.; Sallé, M. Reversible Guest Uptake/Release by Redox-Controlled Assembly/Disassembly of a Coordination Cage. *Angew. Chem. Int. Ed.* **2016**, *55*, 1746–1750.

53. Szalóki, G.; Krykun, S.; Croué, V.; Allain, M.; Morille, Y.; Aubriet, F.; Carré, V.; Voitenko, Z.; Goeb, S.; Sallé, M. Redox-Driven Transformation of a Discrete Molecular Cage into an Infinite 3D Coordination Polymer. *Chem. Eur. J.* **2018**, *24*, 11273–11277.

54. Scott Lokey, R.; Iverson, B. L. Synthetic Molecules that Fold into a Pleated Secondary Structure in Solution. *Nature* **1995**, *375*, 303–305.

55. Ma, J.-P.; Yu, Y.; Dong, Y.-B. Fluorene-based Cu(II)-MOF: a visual colorimetric anion sensor and separator based on an anion-exchange approach. *Chem. Commun.* **2012**, *48*, 2946–2948.

56. Li, K.; Zhao, Y.; Zhang, P.; He, C.; Deng, J.; Ding, S.; Shi, W. Combines DFT and XPS investigation of iodine anions adsorption on the sulfur terminated (100) chalcopyrite surface. *Appl. Surface Sci.* **2016**, 412–421.

57. Although the nature of MOF band gaps remains a debated topic in literature (see: Sippel, P.; Denysenko, D.; Loidl, A.; Lunkenheimer, P.; Sastre, G.; Volkmer, D. Dilectric Relaxation Processes, Electronic Structure, and Band Gap Engineering of MFU-4-type Metal–Organic Frameworks: Towards a Rational Design of Semiconducting Microporous Materials. *Adv. Funct. Mater.* **2014**, *24*, 3885–3896), the bottom-line here is that all three plots consistently yielded similar values for each material and showed that partially oxidized **1a** possessed 0.5–0.6 eV narrower bad gap than **1**.

58. Hao, Z.; Yang, G.; Song, X.; Zhu, M.; Meng, X.; Zhao, S.; Song, S.; Zhang, H. A europium (III) based metal–organic framework: bifunctional properties related to sensing and electronic conductivity. *J. Mater. Chem. A* **2014**, *2*, 237–244.

59. Sun, L.; Park, S. S.; Sheberla, D.; Dinca, M. Measuring and Reporting Electrical Conductivity in Metal−Organic Frameworks: Cd_2(TTFTB) as a Case Study. *J. Am. Chem. Soc.* **2016**, *138*, 14772–14782.

Table of Contents